Impact of Model Physics on Seasonal Forecasts of Surface Air Temperature in the Arctic

QIONG YANG AND MUYIN WANG

Joint Institute for the Study of the Atmosphere and Ocean, University of Washington, Seattle, Washington

JAMES E. OVERLAND

NOAA/Pacific Marine Environmental Laboratory, Seattle, Washington

WANQIU WANG

NOAA/NWS/NCEP/Climate Prediction Center, College Park, Maryland

THOMAS W. COLLOW

NOAA/NWS/NCEP/Climate Prediction Center, College Park, and INNOVIM, LLC, Greenbelt, Maryland

(Manuscript received 19 July 2016, in final form 29 November 2016)

ABSTRACT

The impacts of model physics and initial sea ice thickness on seasonal forecasts of surface energy budget and air temperature in the Arctic during summer were investigated based on Climate Forecast System, version 2 (CFSv2), simulations. The model physics changes include the enabling of a marine stratus cloud scheme and the removal of the artificial upper limit on the bottom heat flux from ocean to sea ice. The impact of initial sea ice thickness was examined by initializing the model with relatively realistic sea ice thickness generated by the Pan-Arctic Ice Ocean Modeling and Assimilation System (PIOMAS). Model outputs were compared to that from a control run that did not impose physics changes and used Climate Forecast System Reanalysis (CFSR) sea ice thickness. After applying the physics modification to either sea ice thickness initialization, the simulated total cloud cover more closely resembled the observed monthly variations of total cloud cover except for the midsummer reduction. Over the Chukchi–Bering Seas, the model physics modification reduced the seasonal forecast bias in surface air temperature by 24%. However, the use of initial PIOMAS sea ice thickness alone worsened the surface air temperature predictions. The experiment with physics modifications and initial PIOMAS sea ice thickness achieves the best surface air temperature improvement over the Chukchi–Bering Seas where the area-weighted forecast bias was reduced by 71% from 1.05 K down to −0.3 K compared with the control run. This study supports other results that surface temperatures and sea ice characteristics are highly sensitive to the Arctic cloud and radiation formulations in models and need priority in model formulation and validation.

1. Introduction

Rapid reduction in Arctic sea ice cover has been observed in the past several decades, especially at the end of the summer melt season in September (e.g., Serreze et al. 2007; Overland and Wang 2013). Accompanying the sea ice cover reduction, the average sea ice thickness of the central Arctic has decreased, primarily due to thin first year ice replacing thick multiyear ice (Kwok and Rothrock 2009).

Fully coupled dynamical models are available to predict Arctic sea ice (Wang et al. 2013; Sigmond et al. 2013; Chevallier et al. 2013). However, these operational prediction systems show only marginally better skill than a linear trend forecast (Blanchard-Wrigglesworth et al. 2015). Seasonal forecasts of surface atmospheric forcing (e.g., air temperature) in the Arctic are also challenging (Wang et al. 2016). Model forecast errors

National Oceanic and Atmospheric Administration Contribution Number 2689 and Pacific Marine Environmental Laboratory Contribution Number 4489.

Corresponding author e-mail: Q. Yang, qiong.yang@noaa.gov

DOI: 10.1175/MWR-D-16-0272.1

are attributed to inadequate representation of important physical processes and uncertainties in initial conditions such as sea ice thickness and subsurface ocean state, which are beyond the influence of atmospheric internal variability (Day et al. 2014). Improved initialization of sea ice thickness has shown to be crucially important for skillful predictions of sea ice and surface air temperature (Day et al. 2014; Msadek et al. 2014; Collow et al. 2015; Bunzel et al. 2016).

Seasonal sea ice plays an important role in the Chukchi–Bering Sea ecosystem, which currently provides half of the U.S. fishery harvest and is home to major populations of U.S. sea bird and marine mammals (Overland and Stabeno 2004; Wang et al. 2012). Wang et al. (2016) evaluated the seasonal predictions of sea ice extent and 2-m surface air temperature from the Climate Forecast System, version 2 (CFSv2), real-time operational forecasts against observations and reanalysis products. They found that the CFSv2 operational forecast overestimated the September sea ice extent and summer surface air temperature over the Chukchi–Bering Seas (Wang et al. 2016). The overestimation in surface air temperature was attributed to the insufficient presence of clouds that caused excessive downwelling solar radiation at the surface during summer and heated up the open water too quickly.

The insufficient cloud cover is mostly due to the disabling of the marine stratus cloud scheme in the CFSv2 operational mode because its use together with the easterly wind bias in the tropical Pacific in the atmospheric component of the model causes a large sea surface temperature (SST) cold bias and greatly weakens the predicted El Niño–Southern Oscillation (ENSO) variability (Saha et al. 2014; Collow et al. 2015). Disabling of the marine stratus cloud scheme essentially turns off the generation of stratus clouds and results in a greater SST warm bias in the high latitudes during warm seasons due to excessive downwelling solar radiation at the surface. The SST warm bias causes rapid sea ice melting. To compensate for this, an artificial upper limit is set for the bottom heat flux from ocean water to sea ice (Collow et al. 2015). These unphysical treatments are justified as ENSO prediction is the dominant concern. Collow et al. (2015) performed CFSv2 hindcast runs with the marine stratus cloud scheme enabled and the upper limit for the ocean–ice heat flux removed. They also conducted hindcast runs with the improved initial sea ice thickness dataset from the Pan-Arctic Ice Ocean Modeling and Assimilation System (PIOMAS; Zhang and Rothrock 2003), which was more consistent with the Ice, Cloud, and Land Elevation Satellite (ICESat; Schutz et al. 2005) observations than the Climate Forecast System Reanalysis (CFSR) sea ice thickness used in the CFSv2 operational forecasts. Collow et al. (2015) established that the skill of September sea ice forecasts was optimized when both the physics modifications and PIOMAS initial sea ice thickness were used in the CFSv2 model. This study is a follow-up work of Collow et al. (2015) and we investigate whether or not these settings also translate to a better representation of the surface energy budget and surface air temperature. The surface energy budget is examined to illustrate the underlying causes of the forecast biases in surface air temperature. We focus on the Chukchi–Bering Seas during summer (July–September).

2. Model and experiments

The CFSv2 is a fully coupled atmosphere–ocean–sea ice–land model (Saha et al. 2014). The atmospheric component is the National Centers for Environmental Prediction (NCEP) Global Forecast System (GFS) model (Moorthi et al. 2001), which has a Gaussian T126 grid (equivalent to $\sim 0.94° \times 0.94°$ grid resolution). The oceanic component is the Geophysical Fluid Dynamics Laboratory (GFDL) Modular Ocean Model, version 4 (Griffies et al. 2004). The zonal resolution is 0.5°. The meridional resolution is 0.25° between 10°S and 10°N and 0.5° poleward of 30°S and 30°N. In between, the meridional resolution gradually decreases from 0.25° to 0.5°. The sea ice component is the GFDL Sea Ice Simulator (Griffies et al. 2004). Its grid resolution is the same as the ocean model. There are three layers for the sea ice model, including two equal layers of sea ice and one layer of snow. In each ice grid, there are five categories of possible sea ice thickness (0–0.1, 0.1–0.3, 0.3–0.7, 0.7–1.1, and >1.1 m). Sea ice dynamics are based on Hunke and Dukowicz (1997) using the elastic–viscous–plastic rheology to calculate ice internal stress. Ice thermodynamics are based on Winton (2000).

We use the same sets of hindcast experiments as those in Collow et al. (2015). The design of the hindcast runs is described briefly in the following. The first set of hindcasts was created using the operational setting with no alterations (CFSv2-ctrl) covering the 2009–13 period and served as the control run for this study. The runs were initialized at 0000 UTC 8–12 March and run for 9-month forecasts to December of the same year. This resulted in five 9-month runs for each year, and a total of 25 runs over the 5-yr period (Table 1). Rapid changes in Arctic sea ice cover over the last decade preclude a meaningful and stable long-term analysis of the Arctic climate, and therefore a shorter hindcast period is used to preserve a relatively constant Arctic state.

The second set of hindcasts (CFSv2-phys) was initialized with the marine stratus clouds scheme enabled and the upper limit on the ocean–ice heat flux removed

TABLE 1. List of the model experiments, whether the run has physics modification or not, source of initial March sea ice thickness, run period, and number of runs for each month.

Model expt	Physics modification	Initial sea ice thickness	Run period[a]	No. of runs per month
CFSv2-ctrl	No	CFSR	2009–13	5 × 5
CFSv2-piomas	No	PIOMAS	2009–13	5 × 5
CFSv2-phys	Yes	CFSR	2009–13	5 × 5
CFSv2-phy-piomas	Yes	PIOMAS	2009–13	5 × 5

[a] For each year, five ensemble runs were initialized at 0000 UTC 8–12 March and run for 9-month forecasts to December.

for the same period as CFSv2-ctrl to analyze the impacts of these changes alone.

The CFSv2 operational system is initialized with the sea ice thickness from CFSR. To investigate the impact of initial sea ice thickness on surface energy budget and air temperature, another set of hindcasts (CFSv2-PIOMAS) was initialized with sea ice thickness distribution generated by the PIOMAS and covered the same period as CFSv2-ctrl and CFSv2-phys (Table 1). Figure 1 shows the difference in initial sea ice thickness between CFSR and PIOMAS in March averaged from 2009 to 2013. In general, CFSR has thicker sea ice over the central Arctic and thinner sea ice near the ice edge over the southern Chukchi Sea, the Beaufort Sea, and the East Siberian Sea along the Russian coast and also over the Canadian Arctic archipelago. On pan-Arctic average, CFSR is about 0.85 m thicker than PIOMAS over the central Arctic, with the largest positive difference (thicker) of 3.8 m over the Beaufort Sea near Banks Island. The largest negative difference in sea ice thickness is found over the southern Chukchi Sea where CFSR is nearly 2 m thinner than PIOMAS.

A final set of hindcasts (CFSv2-phys-piomas) combines both the physics modifications from CFSv2-phys and the use of the initial PIOMAS sea ice thickness from CFSv2-piomas. All hindcasts were compared with the control run (CFSv2-ctrl) to illustrate the impacts of physics modification and initial sea ice thickness on surface air temperature forecasts.

3. Observational data

We utilized the cloud observations from NASA *Cloud–Aerosol Lidar and Infrared Pathfinder Satellite Observations* (*CALIPSO*), 2-m air temperature from the European Centre for Medium-Range Weather Forecasts (ECMWF) interim reanalysis (ERA-Interim), and sea ice concentration from the Hadley Centre Sea Ice and Sea Surface Temperature dataset (HadISST) to evaluate the model simulations. The observational datasets are discussed in more detail below.

a. CALIPSO *cloud observation*

On board the *CALIPSO* satellite is a two-wavelength dual-depolarization lidar (Winker et al. 2007), which is an active sensor and measures the backscattered energy from clouds and thus is not affected by the frequent temperature inversions and difficult light conditions in the Arctic region (Zygmuntowska et al. 2012). It is capable of detecting thin cirrus that account for ~7% cloud fraction in the Arctic (Sassen et al. 2008). *CALIPSO* thus provides a highly accurate measurement of total cloud cover over the Arctic region (Kay et al. 2008; Zygmuntowska et al. 2012). We used *CALIPSO* 5-km level-2 cloud product (version 3) during the period of 2009–13 to derive the mean cloud cover over the Arctic.

b. *ERA-Interim 2-m air temperature*

We used the ERA-Interim gridded 2-m surface air temperature. ERA-Interim is the global atmospheric reanalysis produced by the ECMWF. The data assimilation system includes a four-dimensional variational data assimilation analysis (4D-Var) with a 12-h analysis window (Dee et al. 2011). Instead of estimating the 2-m air temperature by interpolating between the skin temperature and the lowest model temperature as most of

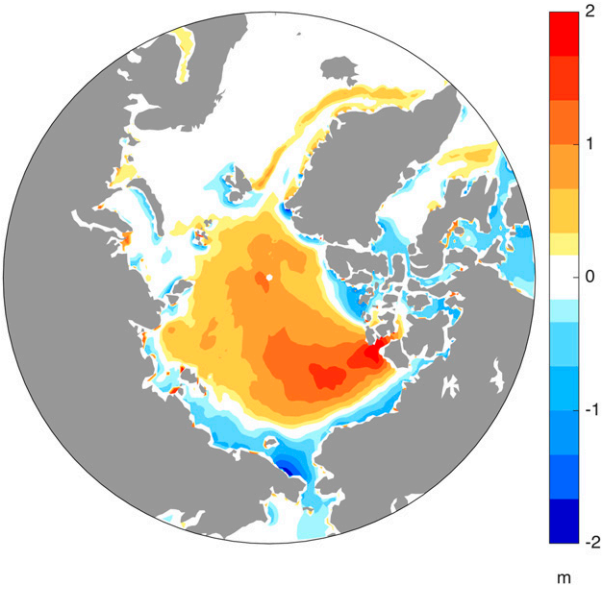

FIG. 1. Differences (m) in March sea ice thickness between CFSR and PIOMAS (CFSR minus PIOMAS) averaged over 2009–13.

the models, ERA-Interim assimilated the observed 2-m air temperature (Dee et al. 2011; Lindsay et al. 2014). As a consequence, ERA-Interim surface air temperature has the smallest biases and is considered to be one of the most reliable reanalyses over the Arctic by evaluating against ground observations (Lindsay et al. 2014). In this study, monthly means with a spatial resolution of 1° × 1° from the reanalysis over 2009–13 were used.

c. *HadISST sea ice*

Monthly mean sea ice concentration was obtained from the Met Office HadISST dataset, version 1 (Rayner et al. 2003). For the period preceding the satellite record, sea ice fields are compiled from historical ice charts from shipping, expeditions, and other activities. After 1979, estimates of sea ice concentration are based on passive microwave satellite retrievals from the Goddard Space Flight Center NASA Team algorithm (Cavalieri et al. 1999). In HadISST, sea ice concentration is defined as the fractional area coverage in each 1° by 1° grid box.

4. Results

a. *Simulated total cloud cover*

The observed total cloud cover from *CALIPSO* exhibits monthly variations during the study period from March to September (black line in Fig. 2). The observed Arctic mean cloud cover increases from 73.5% in March to 82.5% in May and then decreases to 77.8% in July followed by another increase to the maximum of 86.2% in September. The mean total cloud cover is about 80% averaged from March to September over the Arctic region. Note that the area average here is from 60° to 82.5°N to be consistent with the *CALIPSO* satellite polar opening around the North Pole.

Compared with *CALIPSO*, the control simulation CFSv2-ctrl underestimates the total cloud cover with the largest negative bias of 23.4% in June (red line in Fig. 2). Without turning on the marine stratus cloud scheme, the use of improved sea ice thickness initialization alone does not improve the simulated mean cloud cover (CFSv2-piomas experiment; green line in Fig. 2) and has negligible impact on the spatial distribution of total cloudiness (Fig. 5a). After enabling the marine stratus cloud scheme, the total cloud cover increases greatly from 62% in CFSv2-ctrl to 78% in both CFSv2-phys and CFSv2-phys-piomas (blue and magenta lines in Fig. 2) averaged from March to September. The simulated total cloud cover resembles the observed monthly variation very well except for the midsummer reduction seen by *CALIPSO*. The observed midsummer reduction in total cloud cover is mainly attributed to the seasonal cycles of stratocumulus and nimbostratus clouds from the higher

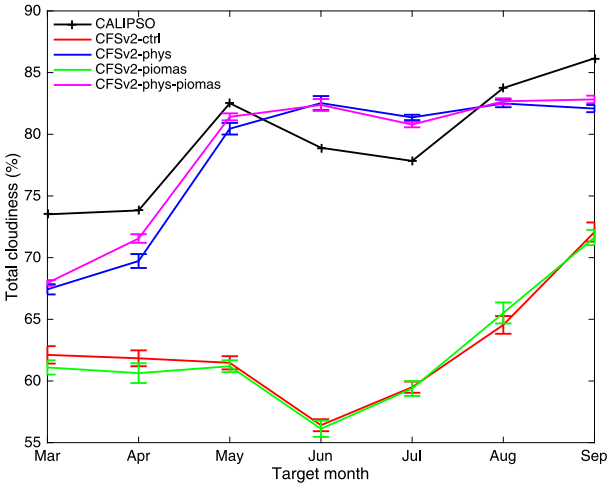

FIG. 2. Monthly mean total cloudiness averaged over the Arctic ocean as a function of target months from March (zero lead time) to September (6-month lead time) derived from CFSv2-ctrl (red), CFSv2-phys (blue), CFSv2-piomas (green), and CFSv2-phys-piomas (magenta) model simulations. For each month, 25 runs are included. Error bars represent ±1 standard deviation from the mean. The cloud observation from *CALIPSO* averaged over 2009–13 is shown in black. Note that the area average here is actually from 60° to 82.5°N due to the *CALIPSO* satellite polar opening.

latitudes poleward of 70°N (Eastman and Warren 2010). Comparing CFSv2-phys-piomas with CFSv2-phys, total cloud cover shows negligible dependence on sea ice thickness initialization especially during summer (magenta and blue lines in Fig. 2). This result is consistent with the recent finding from Taylor et al. (2015) that in the Arctic there is no response of clouds to melting sea ice in summer based on satellite observations. The negligible dependence of cloud cover on sea ice during summer is possibly due to the stabilization of atmospheric boundary layer resulting from sea ice melting, which inhabits the formation of low clouds (Schweiger et al. 2008).

Spatial plots in Figs. 3a–h show that the control simulation has a strong negative bias in total cloud cover over the whole Arctic (Figs. 3a–d). The negative bias is found most significant in June over the Greenland, Barents, Laptev, East Siberian, and Chukchi Seas. After turning on the marine stratus cloud scheme, the simulated cloud cover resembles the *CALIPSO* observations well in August and September (Figs. 3g,h). However, it has positive biases over the Beaufort and Greenland Seas in June and July (Figs. 3e,f). Overall, the simulated total cloud cover is greatly improved by enabling the marine stratus cloud scheme.

b. *Impacts on surface energy budget*

By improving the physics in the model, the total cloud coverage increases by ~26% averaged over July–September

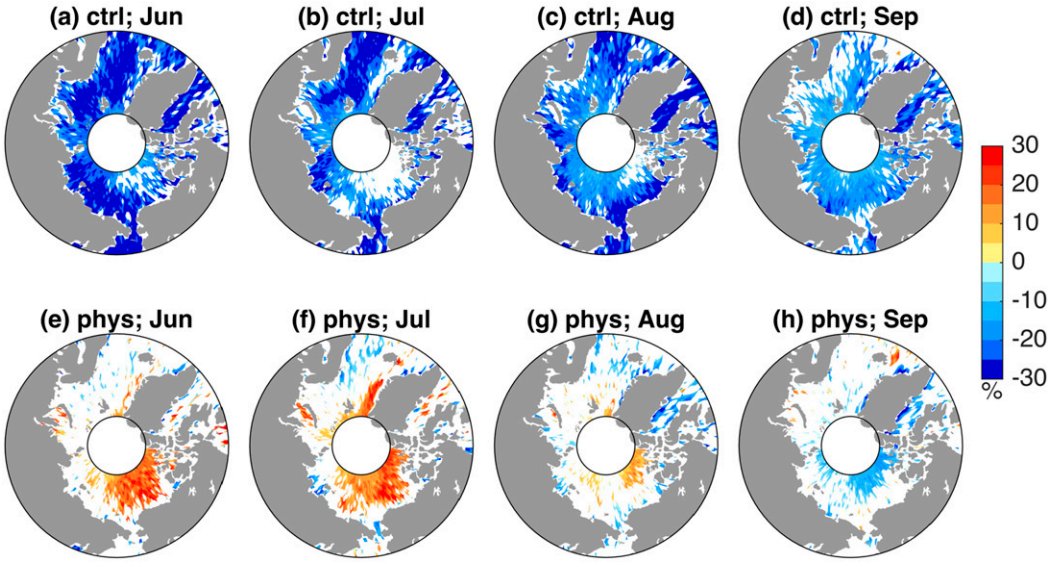

FIG. 3. Differences in total cloudiness (%) compared with *CALIPSO* observation from (a)–(d) CFSv2-ctrl and (e)–(h) CFSv2-phys simulations for June, July, August, and September. All colored fields are significant differences at the 95% level according to the Student's *t* test. The black circle around the North Pole is the *CALIPSO* satellite polar opening at 82.5°N.

and is closer to *CALIPSO* cloud observations. As a result, the downward shortwave radiation at the surface decreases due to clouds reflecting more solar energy back to space (Fig. 4b). The greatest reduction in downward shortwave radiation occurs over the Chukchi, Beaufort, Barents, and Greenland Seas where the total cloud cover is considerably increased (Fig. 4a). Although the downward shortwave radiation decreases, increased sea ice reduction is found over the Greenland, Barents, and Kara Seas (Figs. 4c and 4d). This contradiction is possibly attributed to an increase in ocean–ice heat flux because of the removal of the artificial upper limit on the bottom heat flux from ocean to ice and the positive sea level pressure (anticyclonic) anomaly centered over the Arctic (Fig. 4i). This anticyclonic anomaly with easterlies over the marginal seas increases the transpolar transport of sea ice and may contribute to the increased sea ice reduction over the Greenland, Barents, and Kara Seas seen in Fig. 4d. The faster sea ice reduction decreases surface albedo (Fig. 4e) and reduces the surface reflected shortwave radiation over these regions. The net shortwave radiation (downward shortwave radiation minus upward shortwave radiation) at the surface thus increases over the Greenland, Barents, and Kara Seas but decreases elsewhere due to the reduction in downward shortwave radiation at the surface (Fig. 4f). In response to the increase in cloud cover, net longwave radiation (downward longwave radiation minus upward longwave radiation) at the surface increases over the Arctic as a whole (Fig. 4g). The net downward heat flux, which is the summation of radiative heat fluxes and turbulent latent and sensible heat fluxes, is dominated by net shortwave radiation and exhibits the similar spatial pattern as net shortwave radiation with reductions everywhere except for the enhancement over a strip extending from the eastern Kara Sea all the way to the center of the Greenland Sea where sea ice concentration reduces (Fig. 4h). The simulated 2-m air temperature shows general cooling everywhere except for the warming over the Greenland Sea, where the surface net heat flux increases (Figs. 4h and 4j). The cooling over the central Arctic is contributed from both the reduction in downward shortwave radiation due to the increase of total cloud cover (Figs. 4a and 4b) and the anticyclone that prevents warm southerly flow from entering the interior Arctic (Fig. 4i). The cooling elsewhere is primarily attributable to the reduction in downward shortwave radiation whereas the warming over the Greenland Sea is mainly attributed to the faster ice reduction that reduces surface albedo and increases the net shortwave radiation at the surface.

Figure 5 displays changes of selected fields due to imposing the change of initial sea ice thickness compared with the control run. Changes in total cloud cover and downward shortwave radiation at the surface due to the change of initial sea ice thickness are negligible (Figs. 5a and 5b). CFSv2-piomas is initialized with sea ice thickness from PIOMAS, which has a thinner sea ice over the central Arctic than the CFSR sea ice thickness used in the CFSv2-ctrl (Fig. 5c). Thinner sea ice is more

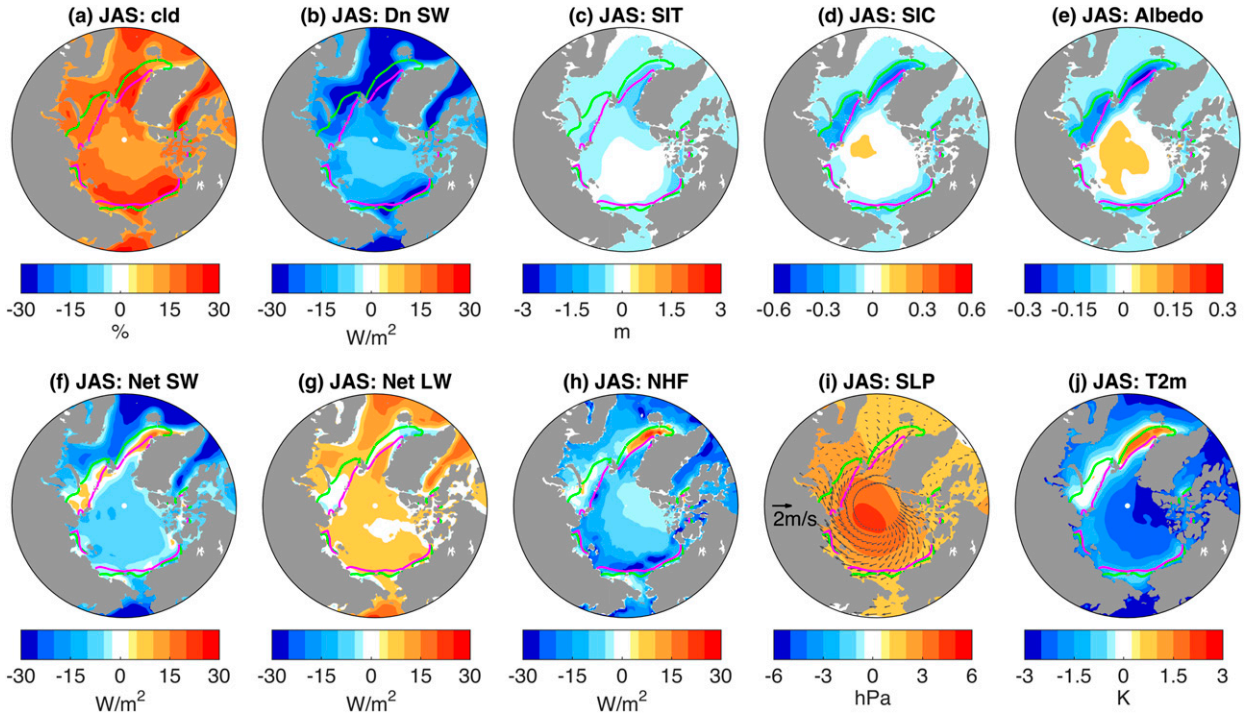

FIG. 4. Differences between CFSv2-phys and CFSv2-ctrl (CFSv2-phys minus CFSv2-ctrl) in (a) total cloud cover, (b) downward shortwave radiative flux at the surface, (c) sea ice thickness, (d) sea ice concentration, (e) surface albedo, (f) surface downward net shortwave and (g) longwave radiative fluxes, (h) surface net heat flux, (i) sea level pressure and 2-m wind, and (j) 2-m air temperature averaged over July–September. The predicted 15% sea ice cover boundary in September from CFSv2-phys and CFSv2-ctrl simulations is plotted in magenta and green, respectively. For (f)–(h), positive (negative) field means more (less) downward flux into surface compared with the control run.

prone to melting. Sea ice concentration is lower over the Chukchi and Greenland Seas and results in the reduction in surface albedo over these regions (Figs. 5d and 5e). In response to the reduction in surface albedo, the net shortwave radiation at the surface increases over the Chukchi and Greenland Seas (Fig. 5f). There is negligible change in net longwave radiation (Fig. 5g). As stated earlier, the surface net flux is dominated by net shortwave radiation and resembles the same characteristics as net surface shortwave radiation (Fig. 5h). No noticeable change in sea level pressure (SLP) is found (Fig. 5i). The 2-m air temperature is warmer over the Chukchi and Greenland Seas compared to the control simulation (Fig. 5j), matching locations of sea ice concentration change.

The CFSv2-phys-piomas experiment exhibits the combined characteristics of the above two experiments and the results are summarized in Fig. 6. Similar to CFSv2-phys, the downward shortwave radiation at the surface decreases due to the increase in total cloud cover (Figs. 6a and 6b). With the faster sea ice reduction over the Greenland, Barents, Kara, and Chukchi Seas, 15% sea ice concentration contour line shifts poleward. The poleward shift of the sea ice edge over the Chukchi Sea is mainly due to the modification of initial sea ice thickness (Fig. 5d) while the poleward shift of the sea ice edge over the Greenland, Barents, and Kara Seas is mainly the result of the model physics modification (Fig. 4d). Compared with the control simulation, the September sea ice extent is reduced by 2.99 million km^2, of which about 1.69 million km^2 is attributed to physics modification alone (CFSv2-phys) and 1.13 million km^2 is attributed to the sea ice thickness initialization alone (CFSv2-piomas). Surface albedo decreases and net shortwave radiation increases over the Greenland, Barents, Kara, and Chukchi Seas (Figs. 6e and 6f). The net longwave radiation increases due to the increase in cloud cover (Fig. 6g). As in CFSv2-phys, an anticyclonic anomaly develops over the central Arctic but with a relatively weaker strength (Fig. 6i). The 2-m air temperature is dominated by the effect of the modified model physics over the Greenland Sea and shows a similar warming pattern as CFSv2-phys (Fig. 4j). Over the Chukchi Sea, the impact of changing the model physics negates the warming seen in CFSv2-piomas resulting in no temperature change in this region. Elsewhere, there is a general cooling as seen in CFSv2-phys (Fig. 6j).

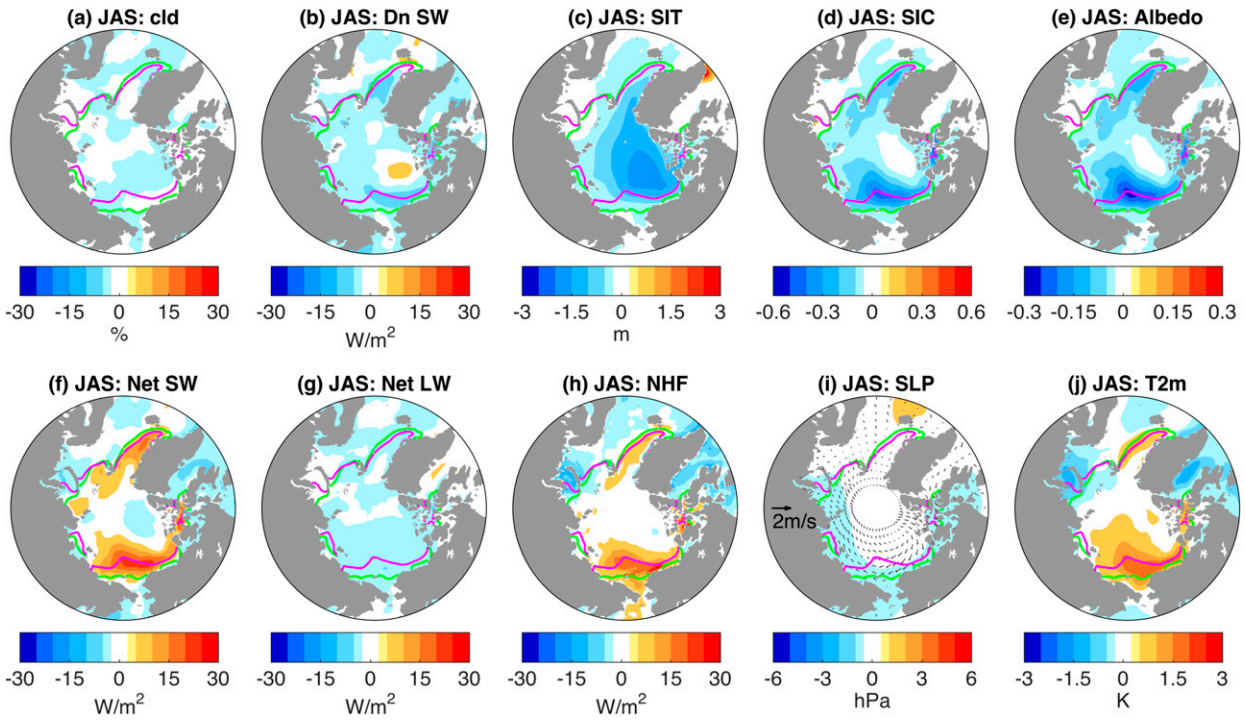

FIG. 5. As in Fig. 4, but for the differences between CFSv2-piomas and CFSv2-ctrl (CFSv2-piomas minus CFSv2-ctrl). The predicted 15% sea ice cover boundary in September from CFSv2-piomas and CFSv2-ctrl simulations is plotted in magenta and green, respectively.

c. *Seasonal forecasts of 2-m air temperature*

We evaluated the predicted 2-m air temperature from the four simulations against ERA-Interim reanalysis to get insights into the impacts of model physics and initial sea ice thickness on seasonal forecasts of 2-m surface air temperature, especially over the Chukchi–Bering Seas. Since the Sea Ice Prediction Network (SIPN; https://www.arcus.org/sipn) produces its annual Sea Ice Outlook (SIO) in June, July, and August, we extended the evaluation of 2-m air temperature from June to September.

The surface air temperature from the control run has warm biases over the southern Chukchi Sea, northern Bering Sea, Norwegian Sea, Baffin Bay, and Labrador Sea, and cold biases elsewhere in summer (Figs. 7a–d). Over the Chukchi–Bering Seas (60°–70°N), the area-weighted forecast bias is about 1.05 K averaged from June to September. It also overestimates the September sea ice extent throughout the Arctic basin compared with the HadISST sea ice observation (magenta and green contours in Fig. 7d). After the model physics modifications, the negative forecast bias in air temperature is reduced over the strip from the eastern Kara Sea to the central Greenland Sea. At the same time, it improves the predicted sea ice extent in the Atlantic sector (Figs. 7e–h). Over the Chukchi–Bering Seas, Norwegian Sea, Baffin Bay, and Labrador Sea, the warm temperature bias in the control simulation is shifted to a cold bias. This is caused by excessive reduction in downward shortwave radiation at the surface (Fig. 4b). Since the total cloud cover is simulated reasonably well compared with the *CALIPSO* observations (Fig. 3), the excessive reduction in surface downward shortwave radiation is attributable to the cloud optical properties and the radiative transfer scheme in the model, which require further research. Over the Chukchi–Bering Seas, the forecast bias in air temperature is reduced down to −0.8 K averaged from June to September. The negative bias in surface air temperature worsens over the central Arctic, which is attributed to both the reduction in downward shortwave radiation due to increase of total cloud cover and the development of anticyclonic circulation that prevents warm southerly flow from entering the interior Arctic as discussed earlier (Fig. 4). The cold biases may be reduced by improving the parameterizations of the cloud radiative scheme, surface turbulent heat fluxes, and ice/snow albedo and increasing the upper ocean vertical resolution to better simulate the sea surface temperature. The simulation initialized with improved sea ice thickness improves the sea ice prediction over the Beaufort, Chukchi, and

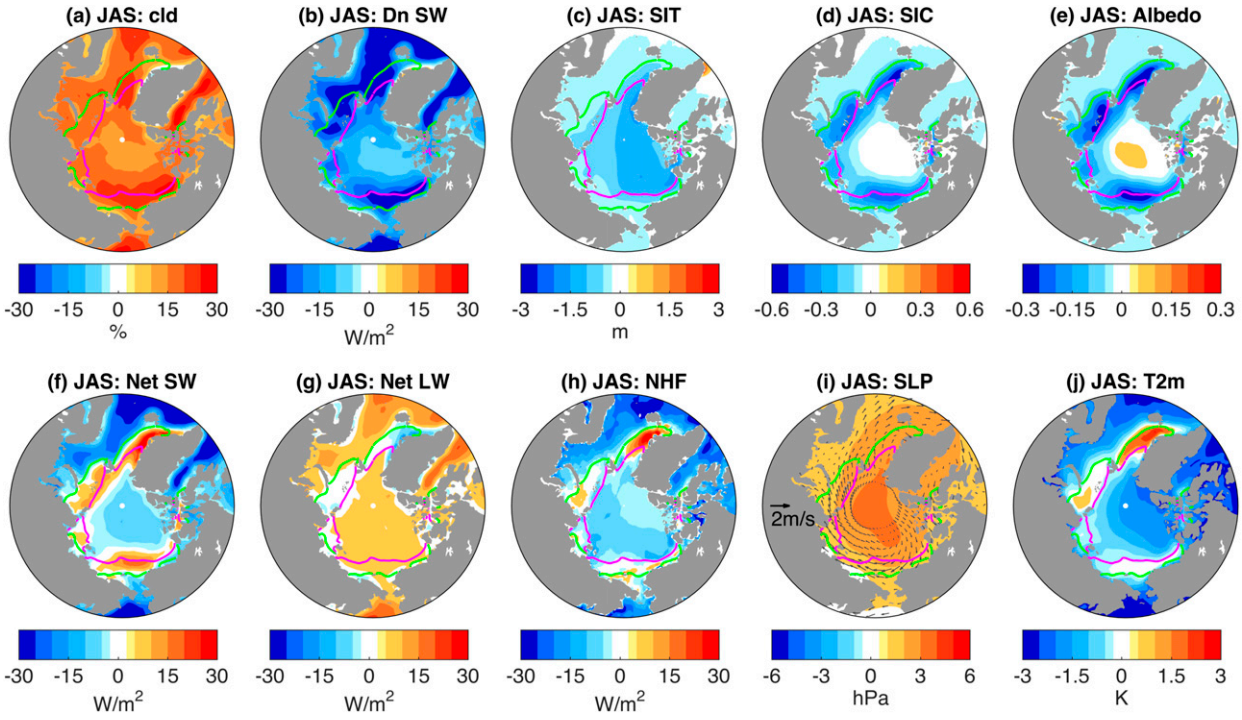

FIG. 6. As in Fig. 4, but for the differences between CFSv2-phys-piomas and CFSv2-ctrl (CFSv2-phys-piomas minus CFSv2-ctrl). The predicted 15% sea ice cover boundary in September from CFSv2-phys-piomas and CFSv2-ctrl simulations is plotted in magenta and green, respectively.

Laptev Seas; however, it worsens the predicted air temperature as the increased sea ice reduction over these regions allows more downward net shortwave radiation at the surface (Figs. 7i–l). The warm bias expands farther north to the central Arctic in September. Over the Chukchi–Bering Seas, the warm bias reaches to 1.46 K averaged from June to September. The effect of model physics modification dominates the effect of changes in initial sea ice thickness in surface air temperature. Combining both the effect of model physics and initial sea ice thickness, the CFSv2-phys-piomas resembles the pattern of CFSv2-phys (Figs. 7m–p). Over the Chukchi–Bering Seas, it has the best prediction of surface air temperature with the forecast bias of ~ -0.3 K averaged from June to September. Compared with the control simulation, it has reduced the forecast bias in surface air temperature by 71%.

5. Summary

In the CFSv2 control simulation, a large warm bias in summer surface air temperature was found over the Chukchi–Bering Seas. This warm bias in surface air temperature was attributed to excessive surface shortwave radiation due to insufficient cloud cover (Wang et al. 2016). After enabling the marine stratus cloud scheme, the simulated total cloud cover increased by ~26%. It simulated the monthly variations well except for the midsummer reduction observed by *CALIPSO*. This overestimation in summer cloud cover was mainly located over the Beaufort Sea in June and July and is subject to future research.

The model physics modifications reduced the negative forecast bias in 2-m air temperature over the strip extending from the eastern Kara Sea to the central Greenland Sea and improved the predicted September sea ice extent in the Atlantic sector. Over the Chukchi–Bering Seas, the forecast bias was reduced by 24% averaged from June to September. The experiment with the improved initial PIOMAS sea ice thickness predicted a better September sea ice edge over the Beaufort, Chukchi, and Laptev Seas. However, it worsened the surface air temperature predictions as the resultant increased sea ice reduction allowed the region of warm temperature biases to expand farther into the Arctic. The experiment with both physics modifications and the use of initial PIOMAS sea ice thickness resembled the pattern of surface air temperature from the physics modifications. It achieved the best surface air temperature predictions over the Chukchi–Bering Seas where the area-weighted forecast bias was reduced by 71% from 1.05 K down to -0.3 K compared with the control run. However, the negative bias worsened

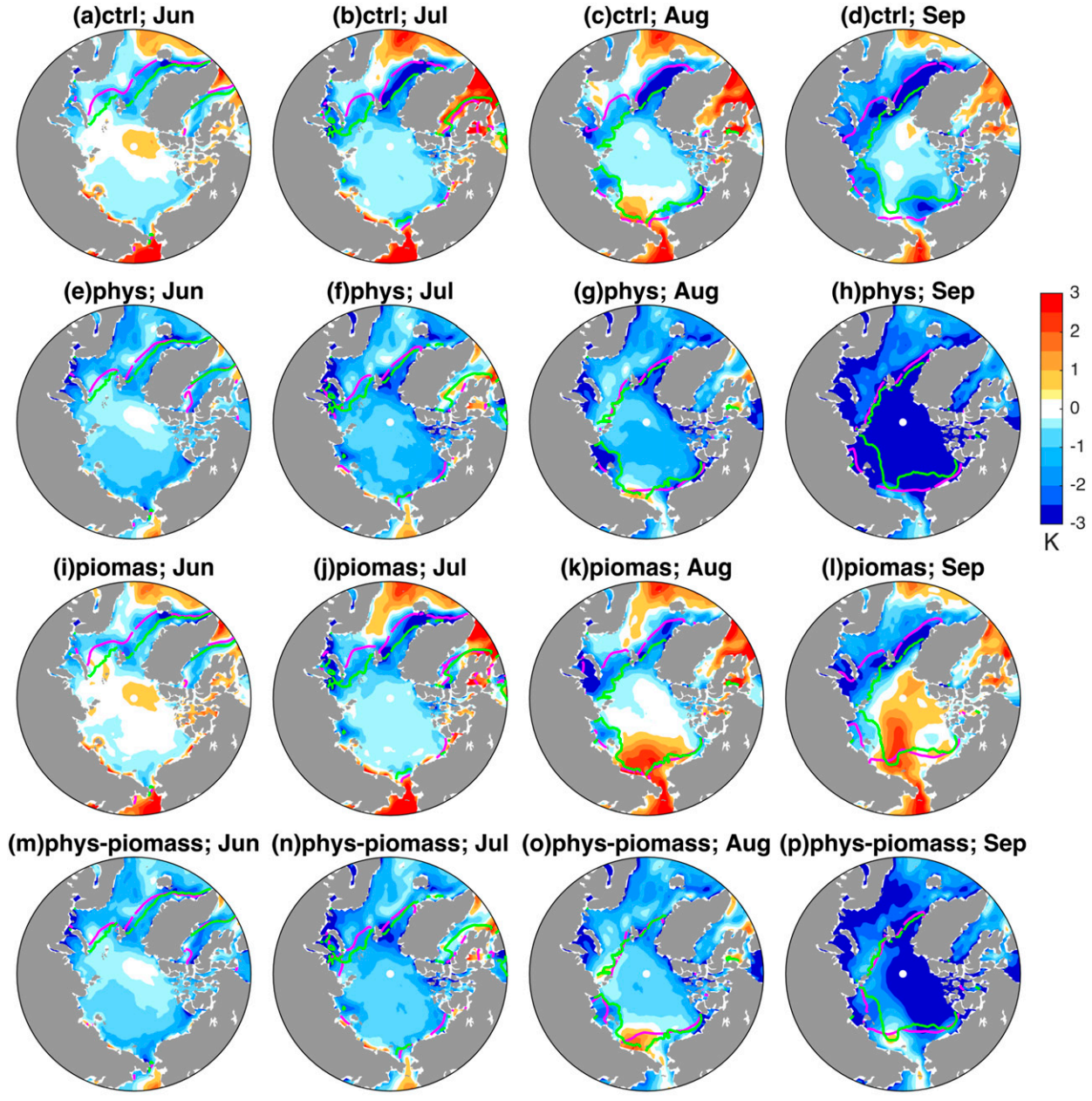

FIG. 7. Differences in 2-m surface air temperature compared with ERA-Interim (CFSv2 minus ERA-Interim) from the (a)–(d) CFSv2-ctrl, (e)–(h) CFSv2-phys, (i)–(l) CFSv2-piomas, and (m)–(p) CFSv2-phys-piomas simulations for (a),(e),(i),(m) June; (b),(f),(j),(n) July; (c),(g),(k),(o) August; and (d),(h),(l),(p) September. Predicted 15% sea ice cover boundary is plotted in magenta for the four model simulations. Observed 15% sea ice cover boundary from HadISST sea ice is plotted in green.

over the central Arctic. This is attributed to both the reduction in downward shortwave radiation due to increase of total cloud cover and the development of anticyclonic circulation that prevents warm southerly flow from entering the interior Arctic. The cold biases may be reduced by improving the parameterizations of cloud radiative scheme, surface turbulent heat fluxes, and ice/snow albedo and increasing the upper ocean vertical resolution to better simulate the sea surface temperature and are subject to further research.

Our study supports other results that surface temperature and sea ice characteristics are highly sensitive to the Arctic cloud and radiation formulations in models, which need priority in model formulation and validation.

Acknowledgments. We thank Met Office Hadley Center and ECMWF for providing data. The NASA Langley *CALIPSO* team provided *CALIPSO* cloud observations. This work is supported by the NOAA Climate Program Office, Arctic Research Program, and by NOAA/OAR under the auspices of the National Earth System Prediction Capability (National ESPC). This publication is partially funded by the Joint Institute for the Study of the Atmosphere and Ocean (JISAO) under NOAA Cooperative Agreements NA10OAR4320148 (2010-2015) and NA15OAR4320063 (2015-2020).

REFERENCES

Blanchard-Wrigglesworth, E., R. Cullather, W. Wang, J. Zhang, and C. M. Bitz, 2015: Model forecast skill and sensitivity to initial conditions in the seasonal sea ice outlook. *Geophys. Res. Lett.*, **42**, 8042–8048, doi:10.1002/2015GL065860.

Bunzel, F., D. Notz, J. Baehr, W. A. Müller, and K. Fröhlich, 2016: Seasonal climate forecasts significantly affected by observational uncertainty of Arctic sea ice concentration. *Geophys. Res. Lett.*, **43**, 852–859, doi:10.1002/2015GL066928.

Cavalieri, D. J., C. L. Parkinson, P. Gloersen, J. C. Comiso, and H. J. Zwally, 1999: Deriving long-term time series of sea ice cover from satellite passive-microwave multisensor data sets. *J. Geophys. Res.*, **104**, 15 803–15 814, doi:10.1029/1999JC900081.

Chevallier, M., D. Salas, Y. Mélia, A. Voldoire, M. Déqué, and G. Garric, 2013: Seasonal forecasts of the pan-Arctic sea ice extent using a GCM-based seasonal prediction system. *J. Climate*, **26**, 6092–6104, doi:10.1175/JCLI-D-12-00612.1.

Collow, T. W., W. Wang, A. Kumar, and J. Zhang, 2015: Improving Arctic sea ice prediction using PIOMAS initial sea ice thickness in a couple ocean–atmosphere model. *Mon. Wea. Rev.*, **143**, 4618–4630, doi:10.1175/MWR-D-15-0097.1.

Day, J., E. Hawkins, and S. Tietsche, 2014: Will Arctic sea ice thickness initialization improve seasonal forecast skill? *Geophys. Res. Lett.*, **41**, 7566–7575, doi:10.1002/2014GL061694.

Dee, D. P., and Coauthors, 2011: The ERA-Interim reanalysis: Configuration and performance of the data assimilation system. *Quart. J. Roy. Meteor. Soc.*, **137**, 553–597, doi:10.1002/qj.828.

Eastman, R., and S. G. Warren, 2010: Arctic cloud changes from surface and satellite observations. *J. Climate*, **23**, 4233–4242, doi:10.1175/2010JCLI3544.1.

Griffies, S. M., M. J. Harrison, R. C. Pacanowski, and A. Rosati, 2004: A technical guide to MOM4. GFDL Ocean Group Tech. Rep. 5, 371 pp.

Hunke, E. C., and J. J. Dukowicz, 1997: An elastic-viscous-plastic model for sea ice dynamics. *J. Phys. Oceanogr.*, **27**, 1849–1868, doi:10.1175/1520-0485(1997)027<1849:AEVPMF>2.0.CO;2.

Kay, J. E., T. L'Ecuyer, A. Gettelman, G. Stephens, and C. O'Dell, 2008: The contribution of cloud and radiation anomalies to the 2007 Arctic sea ice extent minimum. *Geophys. Res. Lett.*, **35**, L08503, doi:10.1029/2008GL033451.

Kwok, R., and D. A. Rothrock, 2009: Decline in Arctic sea ice thickness from submarine and ICESat records: 1958–2008. *Geophys. Res. Lett.*, **36**, L15501, doi:10.1029/2009GL039035.

Lindsay, R. W., M. Wensnahan, A. J. Schweiger, and J. Zhang, 2014: Evaluation of seven different atmospheric reanalysis products in the Arctic. *J. Climate*, **27**, 2588–2606, doi:10.1175/JCLI-D-13-00014.1.

Moorthi, S., H.-L. Pan, and P. Caplan, 2001: Changes to the 2001 NCEP Operational MRF/AVN Global Analysis/Forecast System. NOAA Tech. Bull. 484, 14 pp.

Msadek, R., G. Vecchi, M. Winton, and R. Gudgel, 2014: Importance of initial conditions in seasonal predictions of Arctic sea ice extent. *Geophys. Res. Lett.*, **41**, 5208–5215, doi:10.1002/2014GL060799.

Overland, J. E., and P. J. Stabeno, 2004: Is the climate of the Bering Sea warming and affecting the ecosystem? *Eos, Trans. Amer. Geophys. Union*, **85**, 309–312, doi:10.1029/2004EO330001.

——, and M. Wang, 2013: When will the summer Arctic be nearly sea ice free? *Geophys. Res. Lett.*, **40**, 2097–2101, doi:10.1002/grl.50316.

Rayner, N. A., D. E. Parker, E. B. Horton, C. K. Folland, L. V. Alexander, D. P. Rowell, E. C. Kent, and A. Kaplan, 2003: Global analyses of sea surface temperature, sea ice, and night marine air temperature since the late nineteenth century. *J. Geophys. Res.*, **108**, 4407, doi:10.1029/2002JD002670.

Saha, S., and Coauthors, 2014: The NCEP Climate Forecast System version 2. *J. Climate*, **27**, 2185–2208, doi:10.1175/JCLI-D-12-00823.1.

Sassen, K., Z. Wang, and D. Liu, 2008: The global distribution of cirrus clouds from CloudSat/CALIPSO measurements. *J. Geophys. Res.*, **113**, D00A12, doi:10.1029/2008JD009972.

Schutz, B. E., H. J. Zwally, C. A. Shuman, D. Hancock, and J. P. DiMarzio, 2005: Overview of the ICESat mission. *Geophys. Res. Lett.*, **32**, L21S01, doi:10.1029/2005GL024009.

Schweiger, A. J., R. W. Lindsay, S. Vavrus, and J. A. Francis, 2008: Relationships between Arctic sea ice and clouds during autumn. *J. Climate*, **21**, 4799–4810, doi:10.1175/2008JCLI2156.1.

Serreze, M. C., M. M. Holland, and J. Stroeve, 2007: Perspectives on the Arctic's shrinking sea-ice cover. *Science*, **315**, 1533–1536, doi:10.1126/science.1139426.

Sigmond, M., J. C. Fyfe, G. M. Flato, V. V. Kharin, and W. J. Merryfield, 2013: Seasonal forecast skill of Arctic sea ice area in a dynamical forecast system. *Geophys. Res. Lett.*, **40**, 529–534, doi:10.1002/grl.50129.

Taylor, P. C., S. Kato, K.-M. Xu, and M. Cai, 2015: Covariance between Arctic sea ice and clouds within atmospheric state regimes at the satellite footprint level. *J. Geophys. Res. Atmos.*, **120**, 12 656–12 678, doi:10.1002/2015JD023520.

Wang, M., J. E. Overland, and P. Stabeno, 2012: Future climate of the Bering and Chukchi Seas projected by global climate models. *Deep-Sea Res. II*, **65–70**, 46–57, doi:10.1016/j.dsr2.2012.02.022.

——, Q. Yang, and J. Overland, 2016: Assessment of CFSv2 operational seasonal forecast in the Arctic. *Sea Ice Prediction Network 2016 Workshop*, Palisades, NY, Lamont-Doherty Earth Observatory, Columbia University. [Available online at https://www.arcus.org/sipn/meetings/workshops/may-2016/presentations.]

Wang, W., M. Chen, and A. Kumar, 2013: Seasonal prediction of Arctic sea ice extent from a coupled dynamical forecast system. *Mon. Wea. Rev.*, **141**, 1375–1394, doi:10.1175/MWR-D-12-00057.1.

Winker, D., W. H. Hund, and M. C. Gill, 2007: Initial performance assessment of CALIOP. *Geophys. Res. Lett.*, **34**, L19803, doi:10.1029/2007GL030135.

Winton, M., 2000: A reformulated three-layer sea ice model. *J. Atmos. Oceanic Technol.*, **17**, 525–531, doi:10.1175/1520-0426(2000)017<0525:ARTLSI>2.0.CO;2.

Zhang, J., and D. A. Rothrock, 2003: Modelling global sea ice with a thickness and enthalpy distribution model in generalized curvilinear conditions. *Mon. Wea. Rev.*, **131**, 845–861, doi:10.1175/1520-0493(2003)131<0845:MGSIWA>2.0.CO;2.

Zygmuntowska, M., T. Mauritsen, J. Quaas, and L. Kaleschke, 2012: Arctic clouds and surface radiation—A critical comparison of satellite retrievals and the ERA-Interim reanalysis. *Atmos. Chem. Phys.*, **12**, 6667–6677, doi:10.5194/acp-12-6667-2012.